

Article

A Mach–Zehnder Fabry–Perot Hybrid Fibre-Optic Interferometer for a Large Measurement Range Based on the Kalman Filter

Yixuan Wang , Peigang Yang and Tao Jin *

School of Optical-Electrical and Computer Engineering, University of Shanghai for Science and Technology, Shanghai 200093, China

* Correspondence: jintao@usst.edu.cn

Abstract: To solve the short working distance and small measurement range of an all-fibre interferometer, we proposed a Mach–Zehnder Fabry–Perot hybrid fibre-optic interferometry system based on sinusoidal phase modulation. In this paper, a low-finesse fibre interferometer with a larger linear operating range for displacement measurement is realised using a self-collimating probe and incorporating a Kalman filter-based phase demodulation algorithm. Through experimental comparisons, it is demonstrated that the interferometer proposed in this paper can effectively reduce the phase delay, compensate for the depth of modulation drift, and correct the error due to parasitic interference introduced by the optical path structure through the algorithm. A linear large measurement working range of 20 cm is realised.

Keywords: fibre interferometer; displacement measurement; Kalman filter; parasitic effect

1. Introduction

Laser interferometry is the industry standard in the field of high-precision measurement. Low-energy lasers do not touch and damage the target surface [1,2]. Laser interferometry has the advantages of traceability, high accuracy, and high sensitivity, and has been used on a large scale in various industrial and scientific fields [3]. Taking the typical space light-type Michelson interferometer as an example, its structure development is relatively mature and high-precision, but the beam splitting and interference from the prism group means that the instrument needs to adjust the optical path before use, and the stability of the working platform has high requirements. Based on this, improved Michelson interferometers achieve a larger measurement range and accuracy, but the optical path design is more complex and the calibration is more difficult [4]. The structure of fibre-optic interferometers has basically evolved from space light interferometers. Fibre-optic interferometers use optical fibres as the medium of light transmission, so there is no need to adjust the optical path. Using fibre-optic devices to achieve beam splitting and interference, the standardised fibre-optic interface connection makes the fibre-optic interferometer configuration flexible and can be adapted to a variety of complex spaces.

The mainstream fibre-optic interferometer structures used for displacement measurement are facing the problems of short working distance and small linear measurement range [5]. Therefore, improving the current interferometer structure and designing signal processing algorithms that match the structure to solve the above problems are conducive to improving the measurement performance and realising the miniaturisation of the interferometric displacement measurement system.

For a basic Fabry–Perot (F–P) fibre-optic interferometer, the light reflected from the end face of the fibre is the reference beam, and the measurement beam consists of the portion of the light reflected from the target plane coupled to the end face of the fibre. The interfering signal is measured using the detector via a fibre-optic coupler. The fibre end face and the reflection plane form the F–P cavity, which is located outside the fibre



Citation: Wang, Y.; Yang, P.; Jin, T. A Mach–Zehnder Fabry–Perot Hybrid Fibre-Optic Interferometer for a Large Measurement Range Based on the Kalman Filter. *Optics* **2024**, *5*, 277–292. <https://doi.org/10.3390/opt5020020>

Received: 19 March 2024

Revised: 8 May 2024

Accepted: 13 May 2024

Published: 16 May 2024



Copyright: © 2024 by the authors. Licensee MDPI, Basel, Switzerland. This article is an open access article distributed under the terms and conditions of the Creative Commons Attribution (CC BY) license (<https://creativecommons.org/licenses/by/4.0/>).

and is called the extrinsic type. The extrinsic Fabry–Perot interferometer is suitable for displacement measurements. It has a streamlined structure and is resistant to environmental interference [6]. The intrinsic F–P cavity is placed inside the optical fibre, and depending on the application scenario, such as temperature sensing, pressure sensing, etc., the optical fibre end face is fused to the sensor to form the F–P cavity. Compared with the intrinsic type, the extrinsic type is more suitable for displacement measurements where the cavity distance varies greatly [7]. As the cavity length increases, the intensity of the measurement beam coupled back to the optical fibre decreases rapidly due to the optical fibre divergence angle, resulting in a lower signal-to-noise ratio, which limits the operation of the interferometer when the F–P cavity is used as a displacement sensing unit. This limits the working distance of the interferometer when the F–P cavity is used as a displacement sensing unit. In addition, in a low-finesse F–P cavity, as the measurement beam travels back and forth within the cavity, the optical range difference between the measurement beam and the reference beam is twice as large as the variation in cavity length, further limiting the linear measurement range of the interferometer [8].

Researchers around the world have conducted a lot of research based on the above structure to improve the performance of fibre-optic interferometers for displacement measurement. The existence of the divergence angle at the probe and the alignment deviation between the probe and the target cause the coupling efficiency of the measurement beam to decrease with the working distance, which affects the signal-to-noise ratio of the interfered signal and limits the working distance of the fibre-optic interferometer. Klaus Thurner et al., in their paper, proposed to improve the coupling efficiency of the measurement beam by changing the structure of the F–P cavity. The working distance and signal quality are investigated for different structural designs [9]. While increasing the working distance of fibre-optic interferometers, researchers are also focusing on how to improve the linear measurement range and accuracy of interferometers. Meiners-Hagen proposed to improve the linear measurement range of interferometers up to 145 μm based on the wavelength synthesis of three different wavelengths of laser light [10]. Erik A Moro presented a novel white light F–P interferometer which obtains the displacement information based on the power spectral density estimation, which can be controlled according to the bandwidth, the displacement range, and the accuracy according to the application's requirements [11]. From the above studies, we can see that if we want to achieve a larger range of measurements, researchers usually need to use demodulation algorithms for F–P cavity lengths, such as wavelength tracking [12], and inter-correlation algorithms [13] to incorporate more interference fringes into the calculations. However, the above algorithms are still based on the interference fringes to solve the displacement, the improvement of the linear measurement range is more limited, and the accuracy is still affected by the nonlinearity of the interference signal. B. K. Nowakowski proposed a fibre-optic interferometer structure, whereby a spectrometer monitors the light source and compensates for it in real time while sinusoidally modulating the light source output wavelength, thus avoiding the nonlinear errors introduced by the light intensity modulation due to frequency modulation. The structure achieves a continuous linear measurement range of 25 mm and sub-nanometre accuracy [14]. S. Sharma proposed a structure that introduces phase modulation between the fibre-optic end face and the target to be measured, which does not suffer from the problem of light intensity modulation incidental to light source modulation but introduces a complex alignment mechanism [15]. In order to increase the measuring distance, phase modulation is introduced by adding a reference light path with an electro-optic modulator (EOM) [16], but it also makes the interferometer a Mach–Zehnder structure, which introduces new errors.

Time-varying noise is introduced by the parasitic effect. The noise is affected by external factors. Hence, low-frequency variations in the signal are basically caused by parasitic interference. Then the issue is changed from fixing the parasitic interference to fixing the time-varying Lissajous figure. For Lissajous figure correction, the least squares ellipse fitting approach is frequently employed. Zhang solved the unknown phase shift

problem in the two-step phase shift algorithm using the least squares ellipse fitting algorithm [17]. And, Zhang's 2019 posting uses a two-step random phase retrieval approach based on the Gram–Schmidt (GS) orthonormalisation and Lissajous ellipse fitting (LEF) method (GS&LEF) to obtain relatively accurate phase distribution [18]. Park used the same algorithm to achieve a vibration measurement of 0.4 nm standard deviation in the optical quadrature interferometer [19]. The least squares ellipse fitting approach is capable of achieving respectable accuracy, but it requires a significant amount of computation and choosing the point set to be fitted, which limits its ability to remove time-varying offsets. While numerous gratifying ellipse fitting algorithms have emerged in the field over the decades, such as the Hough-based method [20] and information theory-based methods [21], they are primarily designed for fitting static ellipses and are unsuitable for our specific application. Some machine learning methods, like the deep learning approach [22], data preprocessing [23], and online sequential outlier robust extreme learning machine [24], are also introduced to detect and eliminate outliers. The novelty of their approach lies not only in a different application technique but also in the improvement of other techniques. Some researchers have also introduced a Lissajous figure correction scheme with enhanced dynamic performance. The adaptive modulation algorithm addresses offset concerns by independently collecting the maximum and minimum values of the quadrature signals within a period [25]. Xie simultaneously extracts and compensates for phase delay and modulation depth drift using four sine and four cosine carriers [26]. Guo uses the Kalman filter to eliminate the parasitic interference effect in the external sinusoidal phase-modulating interferometer (ESPMI), which can correct the time-varying error caused by the parasitic interference [27].

In this paper, a different structure of a sinusoidal phase-modulated fibre-optic interferometer system is proposed, where a sinusoidal signal is introduced into the reference arm of the system via an electro-optic modulator (EOM) to modulate the phase, and a probe with a collimating mirror is placed outside of the system for displacement measurement. Compared to the original solution, the interferometer has a flexible built-in configuration that ensures the compactness of the probe and avoids nonlinear errors introduced by the light source modulation. The phase delay, modulation depth drift, and parasitic interferences are analysed in depth, and the phase is solved using a real-time ellipse fitting algorithm based on Kalman filtering. Due to the improvement in the collimated mirror structure on the return light coupling efficiency and the introduction of sinusoidal phase modulation, the system achieves a working distance of 20 cm and a linear measurement range at ambient temperature with repeatability, which can be used as a measurement tool for other research applications.

The rest of the paper is organised as follows. Section 2 describes the Kalman filtering algorithm and simulations are carried out to analyse the performance of the proposal. Validation experiments based on the interferometer of this paper are performed in Section 3.

2. Sensor Structure and Measurement Principle

Figure 1 displays the schematic of the fibre-optic interferometer [16,28]. A monochromatic laser source with a wavelength of 1550 nm is powered with an optical fibre that maintains polarisation. The light travels through the isolator and is then separated by the OC1. The 10% of the laser goes into the reference arm which is equipped with a fibre-optic EOM to change the optical phase sinusoidally, while 90% of the laser enters the measurement arm, and passes through the circulator onto the fibre-optic probe. The fibre-optic probe is a sleeve added to the outside of the fibre-optic cladding and fused to the metal housing together with the collimator mirror. When the target tilt angle increases, the reflected spot will move radially along the end face of the fibre. When the reflected beam is not directly coupled back to the core, thanks to the reflectivity of the cladding and casing, part of the reflected beam deflected to the outside of the core will be reflected by the casing and the cladding back to the F–P chamber; it will then be reflected back to the core via the target to be measured, which is a self-focusing mechanism, and therefore, enhances

the probe's tolerance to the change in the angle of the target to be measured [9]. To achieve nanoscale movement, the target is mounted on a piezo actuator using a capacitive sensor. To travel several millimetres, the piezoelectric moving stage is carried by the step motor. Two routes' lasers recouple in the OC2, and an InGaAs photodiode detector picks them up. Through the use of direct digital frequency synthesis (DDS), the digital-to-analogue converter (DAC) transforms the sinusoidal digital signal produced by the FPGA into a modulation carrier, which it then sends to the EOM. The displacement is retrieved with the use of the modulation carrier and demodulation signal in accordance with the PGC algorithm implemented on FPGA. The fibre paths are all fixed inside a container to withstand additional disruption.

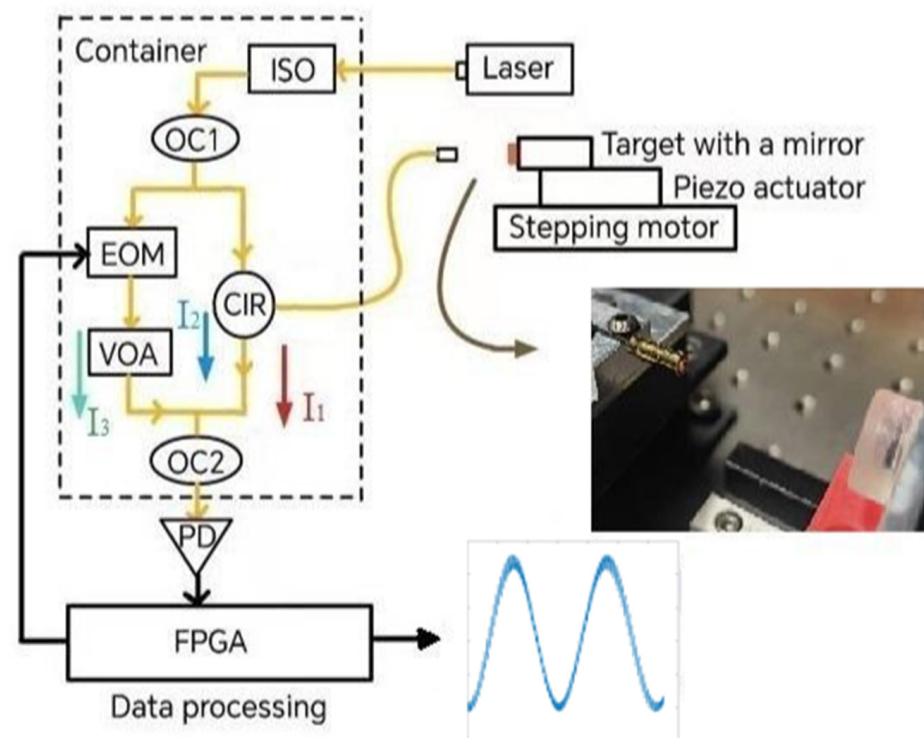


Figure 1. Schematic diagram of the all-fibre low-finesse F-P interferometer with phase modulation. ISO: optical isolator; OC1: a 90:10 optical coupler; OC2: a 50:50 optical coupler; EOM: electro-optic modulator; VOA: variable optical attenuator; CIR: optical circulator; PD: photodiode detector; FPGA: field programmable gate array.

The interferometric system calculates the phase difference by comparing the optical path difference between the measurement beam and the reference beam. In the experimental environment, the drift of the EOM excitation current leads to the drift of the modulation depth, and factors such as the measurement system optical transmission and circuit delay introduce phase delay terms to the quadrature signals. If the quadrature signals are a directly inverse tangent operation, it will introduce errors and lead to dephasing failure. The interference frequency between the measurement arm and stray light is much lower than the modulation frequency and is filtered out after mixing and filtering, while the interference between the reference arm and stray light is modulated, resulting in a demodulated quadrature signal that will contain the offset caused by stray light. Due to the existence of Mach-Zehnder structures, the reference beam not only provides a modulated reference light but also introduces additional interference caused by environmental factors, such as temperature drift, pressure changes, and platform vibration, which affect the system and

cause changes in the optical path difference. The interferometric signal after introducing interference is [29]

$$\begin{aligned} I_t &= \left| I_c + I_l + \sum_{j=1}^n I_j \right|^2 \\ &\approx A_c^2 + A_l^2 + 2A_c A_l \cos(\varphi_c - \varphi_l) \\ &\quad + \sum_{j=1}^n 2A_c A_j \cos(\varphi_c - \varphi_j) + \sum_{j=1}^n 2A_l A_j \cos(\varphi_l - \varphi_j) \end{aligned} \quad (1)$$

After mixing the interference signal with the fundamental frequency and double frequency of the sinusoidal modulation signal, a set of quadrature signals $P(t)$, $Q(t)$ with varying amplitude and offset can be obtained through low-pass filtering. To obtain the phase solution, the tangent of $P(t)$, $Q(t)$ is calculated. When the phase delay $\theta_c \neq 0$ and the modulation depth deviates by 2.63 rad [29], an error term caused by amplitude and offset will also be obtained in addition to the phase to be solved.

$$P(t) = LPF[I(t) \cdot \cos(\omega_t t)] = X_0(t) \sin[\varphi(t)] + X_1(t) \quad (2)$$

$$Q(t) = LPF[I(t) \cdot \cos(2\omega_t t)] = Y_0(t) \cos[\varphi(t)] + Y_1(t) \quad (3)$$

The obtained $P(t)$ and $Q(t)$ are combined into a functional expression conforming to the elliptic equation according to the form of their mathematical expression function.

$$pP^2(t) + qQ^2(t) + rP(t) + sQ(t) + e = 0 \quad (4)$$

This elliptic equation represents the received interference signal. We use an algorithm that adds Kalman filtering to the traditional PGC-Arctan process, and the prediction process and update process of the Lissajous figure parameters formed using the orthogonal components are based on the error between the predicted value and the measured value to update the optimal estimation results in real time, so as to realise the estimation of the system's true value in the presence of noise interference and to avoid the interference from entering into the arctangent operation. In this way, the effects of phase modulation depth drift, phase delay, and parasitic interference are reduced. The concept of linear discrete Kalman filtering is introduced and the process equation of Kalman filtering is presented. The elliptic parameters are required for the Kalman filtering equation, and P and Q are corrected according to the filtering results to eliminate errors and obtain the correct interference signal.

$$x_{m+1} = F_{m+1} \times x_m + v_{m+1} + w_{m+1} \quad (5)$$

$$z_{m+1} = G_{m+1} \times x_m + u_{m+1} \quad (6)$$

Equations (5) and (6) are the state equation and observation equation of the Kalman filter. F_{m+1} is the state transfer matrix; v_{m+1} is the control matrix; w_{m+1} is the process noise; z_{m+1} is the system observation vector; G_{m+1} is the observation matrix; and u_{m+1} is the observation noise, usually Gaussian white noise. The observation equation obtained after discretising P_m and Q_m is used as the input, where m is the number of samples. $X_0(t)$, $X_1(t)$, $Y_0(t)$, and $Y_1(t)$ are treated as constants [29]; p_m , q_m , r_m , s_m , and e_m are the discretised elliptic parameters.

$$L_m = l(x_m, P_m, Q_m), x_m = [p_m q_m r_m s_m e_m]^T \quad (7)$$

Since L_m is a nonlinear model and the discrete Kalman filter describes a linear model, the linearisation is expanded for each sampling point in the observation model. G_m is a linearised observation model and R_m is covariance.

$$G_m = \frac{\partial L_m}{\partial x_m} \quad (8)$$

$$R_m = \partial \left[\left(\frac{\partial L_m}{\partial P_m} \right) + \left(\frac{\partial L_m}{\partial Q_m} \right) \right] \tag{9}$$

Based on the given system observation model and basic equations, the prediction equation and update equation of the Kalman filter in Figure 2 are used to iteratively calculate the optimal estimated state vector \tilde{x}_m .

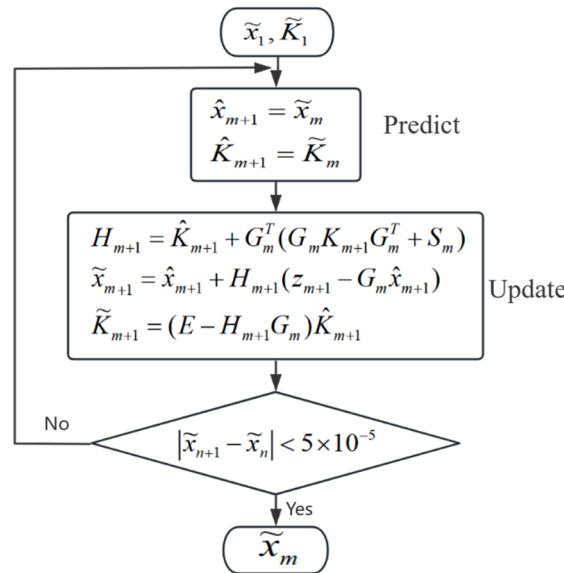


Figure 2. Schematic of Kalman filter iteration process. Where \hat{x}_{m+1} and \tilde{x}_{m+1} , respectively, represent the $(m + 1)$ st prior state estimation vector and optimal state estimation vector predicted from the m th optimal state estimation vector. \hat{K}_{m+1} and \tilde{K}_{m+1} represent the prior estimation covariance matrix and optimal estimation covariance matrix for the $m + 1$ st order. H_{m+1} represents the gain matrix of the $m + 1$ st Kalman filter and represents the weighted matrix of the residual between the actual observation value and the prior estimate value. E is the identity matrix.

According to the five basic equations in Figure 2, during the iterative computation, the state vector \tilde{x}_m to be solved (elliptic parameter) is considered a stable matrix when $|\tilde{x}_{n+1} - \tilde{x}_n| < 5 \times 10^{-5}$, the iteration from the m th to the $(m + 1)$ st, can be completed. By substituting the values in \tilde{x}_m into Equation (10), the amplitude and bias of the discrete quadrature component can be obtained.

$$\begin{cases} X_0(m) = \sqrt{\tilde{q}_m} \\ Y_0(m) = \sqrt{\tilde{p}_m} \\ X_1(m) = -\tilde{r}_m / 2\tilde{p}_m \\ Y_1(m) = -\tilde{s}_m / 2\tilde{q}_m \end{cases} \tag{10}$$

where $\tilde{p}_m, \tilde{q}_m, \tilde{r}_m, \tilde{s}_m$, is the elliptical parameter after iterative calculation. According to Equation (11), the measured phase that eliminates the effects of carrier phase delay and modulation depth fluctuations can be obtained.

$$\varphi(t) = \arctan \left[\frac{P(t) - X_1(t)}{X_0(t)} \cdot \frac{Y_0(t)}{Q(t) - Y_1(t)} \right] \tag{11}$$

Figure 3 shows the optimal estimation results of the Kalman filter for the quadrature signal amplitude and bias during the ellipse fitting process. It can be seen that after about 1/4 of the cycle, the filtering results start to converge and accurate quadrature component parameters are obtained. Meanwhile, compared with the ellipse fitting algorithm based on the least squares method, the output of the Kalman filter is a dynamic optimal estimation,

which changes according to the real-time measurements and, thus, can be used to solve the displacement results in real time. Figure 3c demonstrates this performance of the Kalman filter, simulating a slowly varying amplitude phase based on the previously mentioned interference model, and Figure 3d shows the results of the optimal estimation. Through simulation, the effectiveness of Kalman filter correction for ellipse parameter fitting and its necessity in this study are verified.

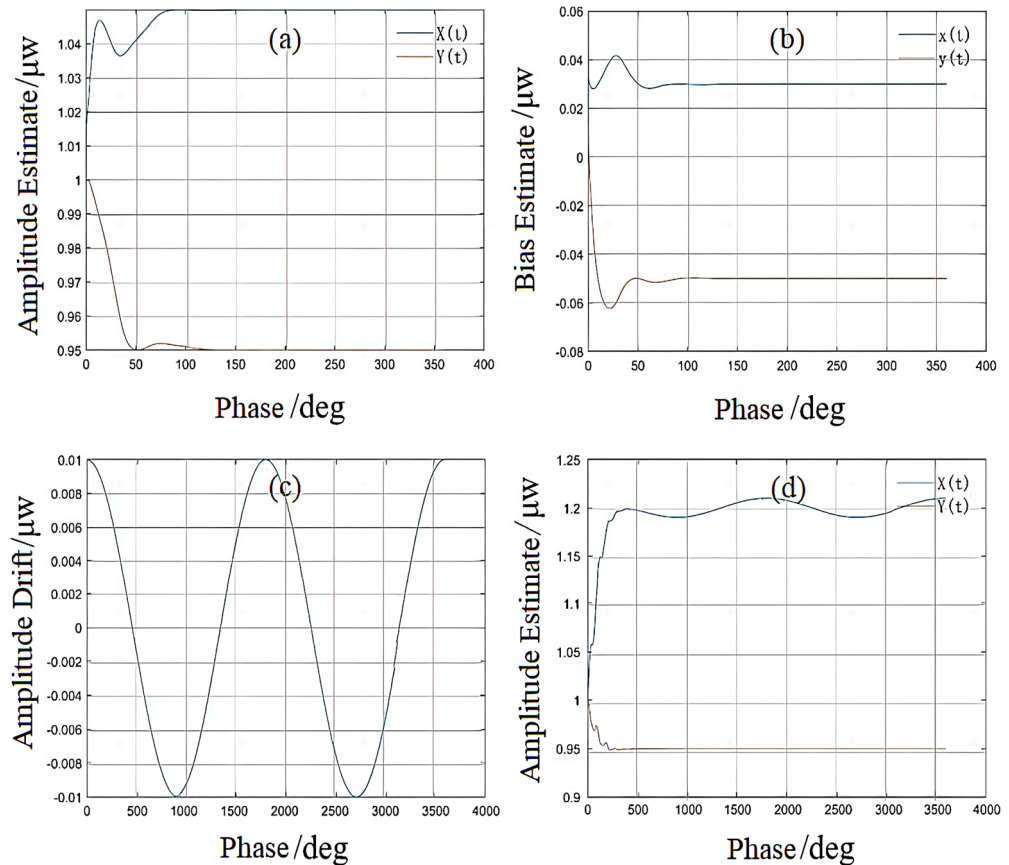


Figure 3. Kalman filter estimation results. (a) Quadrature signal amplitude estimate. (b) Quadrature signal bias estimate. (c) Amplitude drift of $X(t)$. (d) Estimated value of amplitude for quadrature signals.

3. Experiments and Processes

In Guo's paper, three methods of least squares ellipse fitting correction, coherence length control, and Kalman filter correction were used in the experiments for parasitic interference error correction. Table 1 presents a comparison of the elliptical fitting correction, coherence length control, and Kalman filter correction approaches. By lowering the measurement standard deviation from 10.1 nm to 1.8 nm, the Kalman filter correction approach clearly had the best suppression effect on parasitic interference, demonstrating the algorithm's efficacy [27].

Table 1. Performance of three error correction methods during dynamic measurements [27].

Error Correction Method	Peak Value/nm	Standard Deviation/nm
Coherence length control	36.2	10.1
Ellipse fitting correction	12.0	3.5
Kalman filter correction	8.6	1.8

Here, several sets of comparative tests are conducted to verify that the phase generated carrier (PGC) demodulation algorithm with the addition of Kalman filtering performs better than the previous fibre-optic interferometric system in displacement measurement, and the resolving power of the interferometer is also calibrated to obtain the measurement capability in general environment.

The detection target moves with the piezoelectric displacement stage at a uniform speed, the measurement signal is modulated with the phase carrier and collected using the detector, the modulated interference signal is processed using the principle of phase-locked amplification, and the first-order and second-order harmonic components are extracted from it using the finite-length impulse response (FIR) filter [30], and the results of the displacement and the PGC solving are shown in Figure 4, which shows that the PGC phase demodulation algorithm based on Kalman filtering can solve the real displacement of the object efficiently. The real displacement of the object can be solved effectively. After stabilisation, the error is sinusoidal with an amplitude of less than $0.001 \mu\text{m}$, which is due to the fact that the Kalman filter itself is in the process of continuous iterative estimation, which is dynamic.

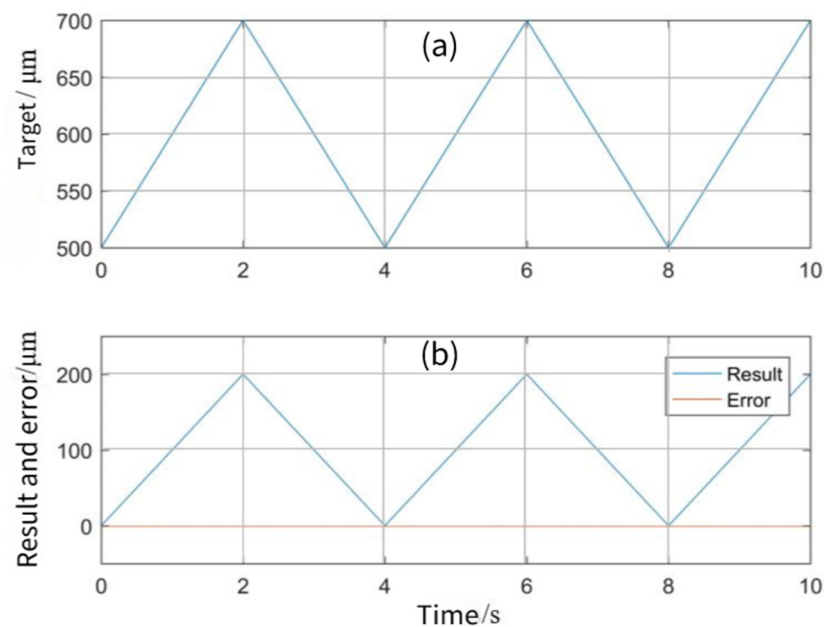


Figure 4. Displacement measurement results: (a) target displacement; (b) displacement solution results and solution error.

When dephasing the results, phase delay and phase modulation depth drift as well as parasitic interference introduce different amplitude variations and bias variations, respectively, in the quadrature signals used for arctangent. Here we continue to discuss the effects of disturbances such as phase delay, modulation depth drift, and parasitic interference during signal processing, as well as validate the ability of the Kalman filter-based dephasing algorithm to correct errors.

The effect of the presence of parasitic interference due to end face-reflected light, etc., on the quadrature signals and demodulation results is experimentally verified with the Kalman filter correction method to correct for bias variations with the final demodulation capability. Parasitic interference is mainly caused by multiple reflections from high-reflectivity targets, as well as temperature drift, the vibration of the working abutment, pressure changes, and other factors introduced in the Mach–Zehnder structure of the interferometer in this paper. The mathematical model is based on the Equation (1). The parasitic interference of the mixture of interfering signals with different frequencies

and intensities, and the amplitude of the systematic parasitic interference in the general environment was measured experimentally at 0.2 rad, which is equivalent to 50 nm.

The results of Kalman filtering to correct the effect of parasitic interference are shown in Figure 5. Figure 5a,b shows the effect of parasitic interference on the Lissajous figure, and it can be seen that the Lissajous figure in the direction of y-axis (in fact, the x-axis is also biased) at different moments will have different offsets, which is due to the fact that the parasitic interference introduces bias to the orthogonal components, respectively, and Figure 5b is the signal data after correcting for the error, and the optimally estimated bias is in line with the actual bias after Kalman filtering. It can be seen that the optimally estimated bias after Kalman filtering is consistent with the actual bias, which can effectively eliminate the parasitic interference in the modulation and demodulation process of the PGC method.

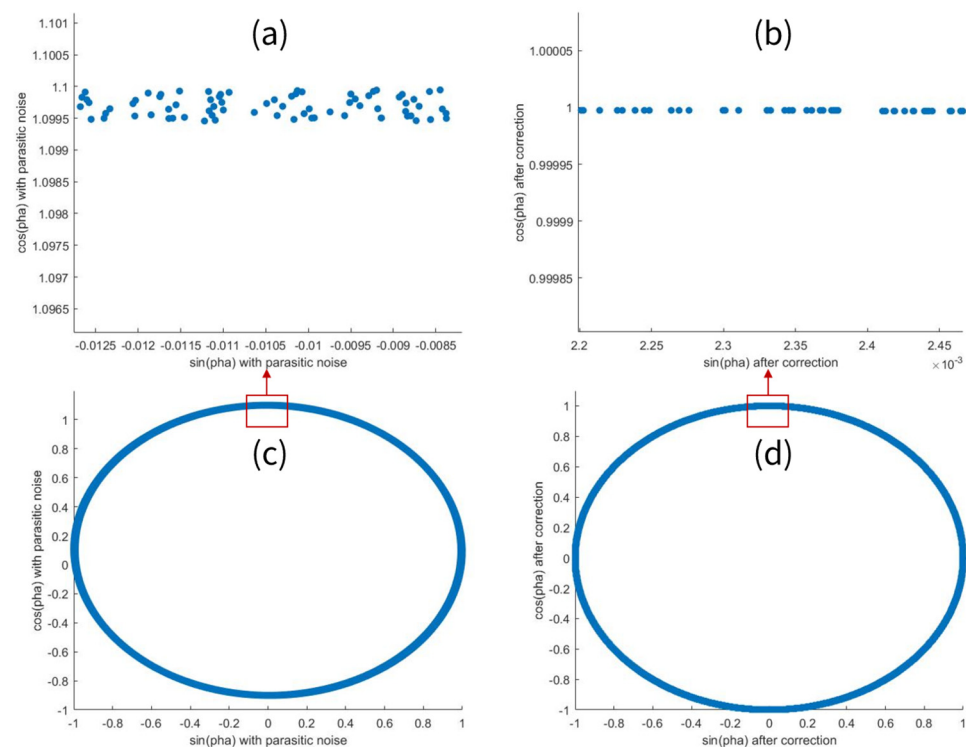


Figure 5. The Lissajous figure of quadrature signal after amplitude change. (a) Quadrature signal before correction of bias; (b) Quadrature signal after correction of bias; (c) The Lissajous figure under the influence of phase delay and modulation depth drift; (d) The Lissajous figure after the demodulation algorithm to correct for the amplitude change.

Figure 5c shows the Lissajous figure formed via the quadrature signals after the amplitude change under the influence of phase delay and modulation depth drift. It can be seen that the existence of phase delay and modulation depth drift will introduce different amplitude terms in the quadrature signals, in which $X(t) = 0.0175$, $Y(t) = 0.0595$. The quadrature signals from the Lissajous figure shape deviate from the quadrature figure. If the quadrature signals directly execute the inverse tangent operation, it will introduce the periodic error, the range of error by the phase delay, and the modulation depth drift of the specific value of the decision. In some specific values, there is a zero value for the denominator of the inverse tangent, which can lead to the failure of the solution. Figure 5d shows the Lissajous figure fitted using the quadrature signal after the amplitude change is corrected with the demodulation algorithm. Firstly, the amplitude is optimally estimated using the Kalman filter, then the amplitude of $P(t)$, $Q(t)$ is corrected according to Equation (10), the Lissajous figure fitted using the quadrature signal after the correction is a positive circle, and the inverse tangent operation is performed to avoid the periodic error in the figure.

In Figure 6a, it can be seen that the interference signal received by the photodetector varies with time. Since the phase of the cosine component of the signal can exist greater than 2π , a dip in the signal plot is observed in Figure 6a. From the Fourier expansion of the interferometric signal in Figure 6b, it can be seen that there are multiple peaks in the frequency domain signal, which proves the existence of multiple order harmonic components in the detected interferometric signal. Through the displacement solving results in Figure 6c, it can be observed that the measured displacement shows a linear change with time. The interferometer in this paper, as can be seen in Figure 6c, increases the linearity of the working range to 200 mm. By comparing bare optical fibre, it can be seen that the linearity of the interferometer is always well maintained within the working range. This experiment provides strong support for the further development and application of interferometer technology and helps to promote research and application in related fields.

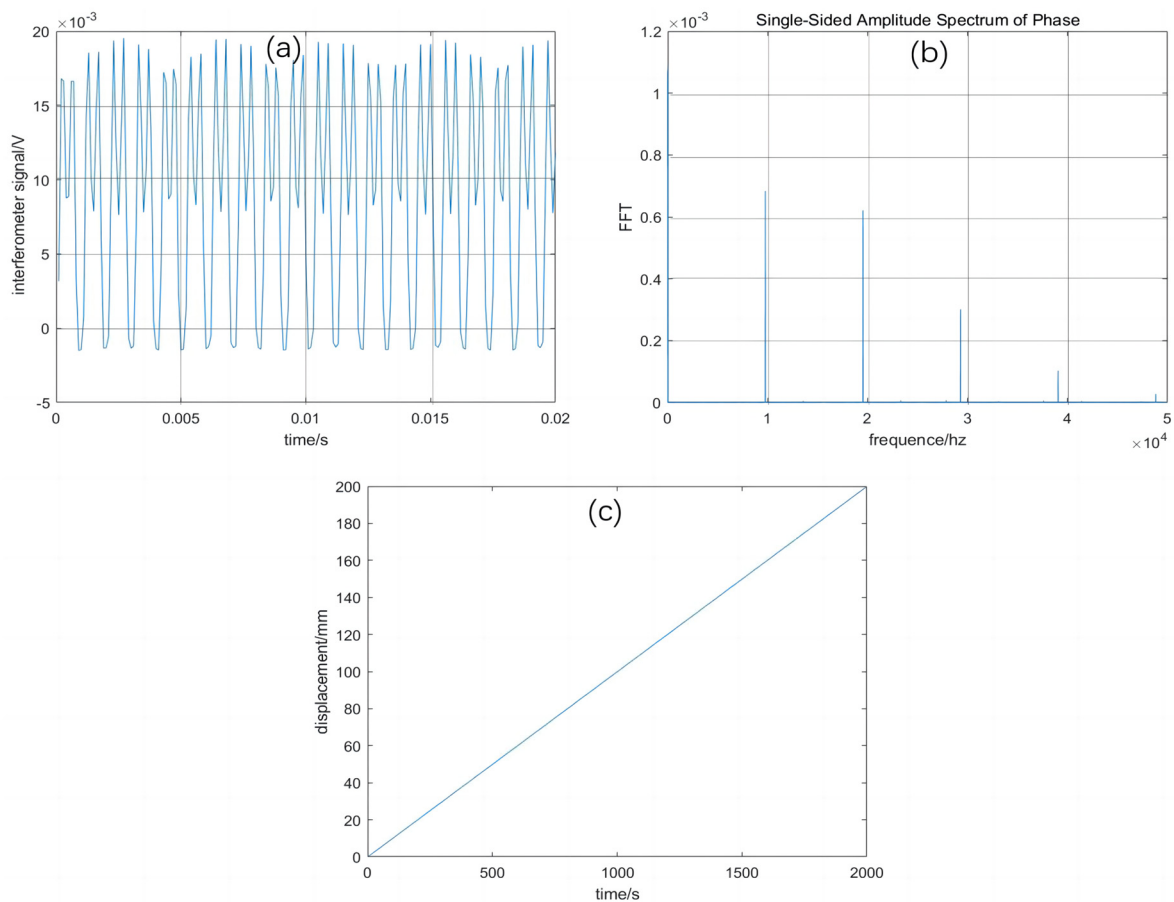


Figure 6. The displacement measurement experimental data and displacement solution results; (a) the time-domain interference signal; (b) the frequency-domain interference signal; and (c) the displacement solution result.

It is proved that the interferometer in this paper can ensure the displacement measurement works in the working range of 20 cm and solves the correct displacement. These results validate the functionality and performance of the interferometer for the intended application.

To ensure the reproducibility of the interferometer in long-distance measurements, a rigorous experimental setup was employed, involving repeated trials and meticulous data analysis. The experimental procedure entailed the linear displacement of the stepper motor within the range of 5 mm to 45 mm. However, to mitigate potential errors arising from mechanical characteristics, data collection was focused on the segment spanning 10 mm to 40 mm. Seven iterations of the experiment were conducted, each yielding a

dataset of displacement measurements. These datasets were subjected to thorough analysis and statistical treatment to extract meaningful insights. Through the careful fitting of the data points, a straight-line model was established, capturing the underlying trend of the measurements. In Figure 7a, the results of the fitting process are presented, accompanied by a root mean square error (RMSE) of 0.0013 μm . This metric serves as a quantitative indicator of the fidelity of the fitted model to the experimental data. Moreover, to provide a closer examination of the fitting accuracy, Figure 7b offers a zoomed-in view, revealing minimal y-axis deviation, typically below 10 nm, along the fitted straight lines. It is noteworthy that the observed y-axis deviation is primarily attributed to the inherent resolution limitations of the stepping motors rather than intrinsic flaws in the interference system. This distinction underscores the meticulous attention paid to isolating and understanding sources of measurement uncertainty. Furthermore, the exemplary linearity exhibited in the fitted lines corroborates the interferometer's robust reproducibility across varying displacement ranges. This characteristic is pivotal in ensuring the reliability and consistency of measurements, essential for scientific and industrial applications demanding high precision. In essence, the comprehensive analysis and optimisation efforts undertaken in this experiment underscore the commitment to achieving accurate and reproducible long-distance measurements using the interferometer setup.

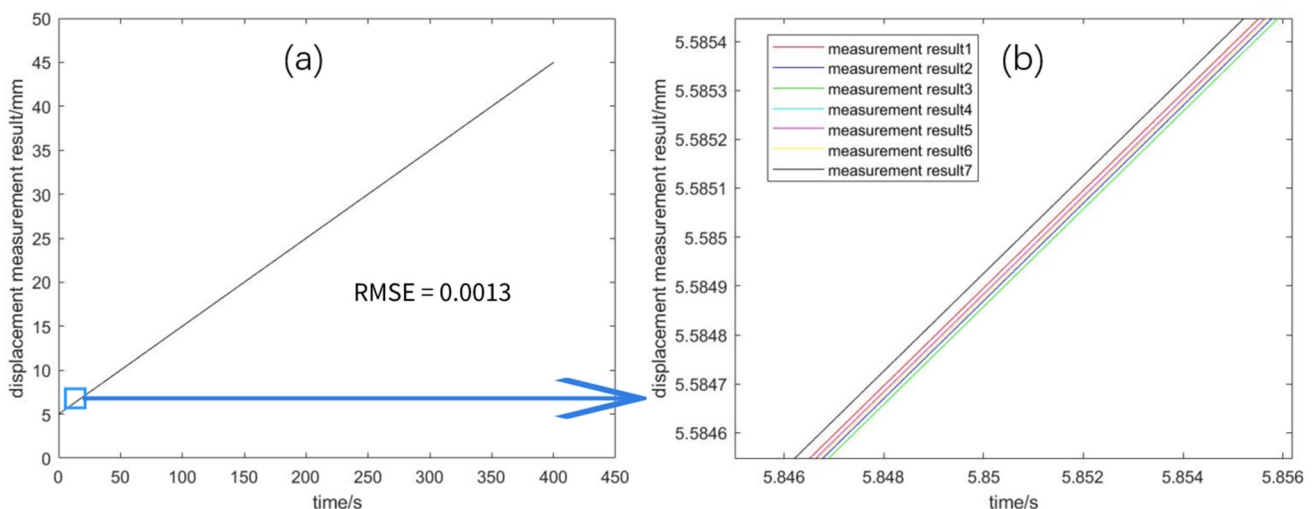


Figure 7. Reproducibility experiments: (a) linear fit results from 5 mm to 45 mm and (b) linear fit results after zooming in to a 0.001 mm range.

The interferometer's displacement measurement resolving power underwent calibration through step displacement experiments shown in Figure 8. The process began with deactivating the controller of the nano-displacement stage, allowing it to stabilise over several days to mitigate the creep effect commonly associated with piezoelectric ceramics. Subsequently, step displacement experiments were meticulously conducted.

The nano-displacement stage served to execute five step displacements, each with a precise step size of 10 nm. Following each displacement, sufficient time was allocated for stabilisation before measurements were taken. The comprehensive results of these system measurements are graphically represented in Figure 9. The measurement outcomes are clearly displayed, revealing the system's remarkable resolution, exceeding 10 nm under normal environmental conditions. This calibration process, including the pre-stabilisation period and step displacement experiments, underscores the meticulous approach employed to ascertain and validate the interferometer's high-resolution capabilities. This calibration process not only validates the interferometer's technical specifications but also instils confidence in its ability to deliver precise and reliable measurements in real-world scenarios.

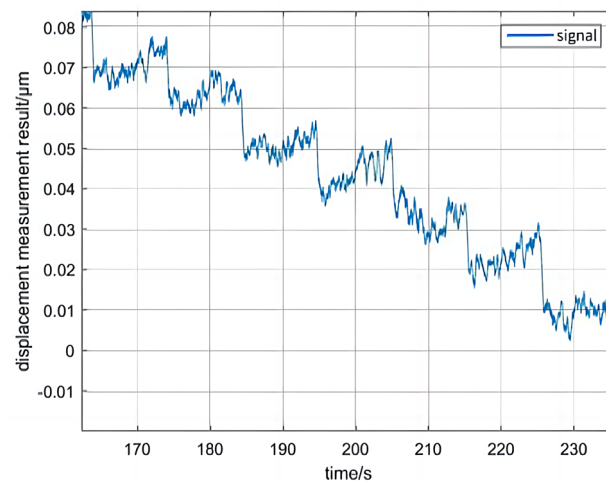


Figure 8. Experimental results of step displacement.

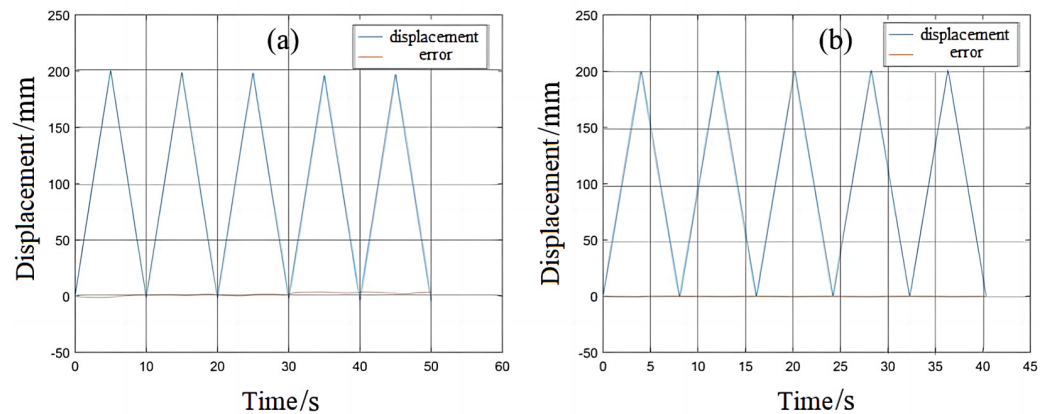


Figure 9. The suppression effect on the measurement error of parasitic interferences. (a) The phase delay and modulation depth drift extraction and compensation method based on four sine and four cosine carriers proposed by Xie [26]; (b) the PGC phase demodulation scheme based on Kalman filtering.

In order to demonstrate the effect of the interference system on the suppression of parasitic interference in this paper, the experiments compare the measurement displacement errors of two different demodulation algorithms, using collimated probes to reduce the nonlinear errors caused by the attenuation of the return optical coupling, and show the measurement errors of the same measurement displacement before and after the parasitic interference correction.

The stepper motor drives the target to linearly displace 20 cm from the initial position, and the modulated interference signal received by the photodetector is shown in Figure 9. As can be seen from the figure, Xie's method is able to complete the measurements but produces errors in the case of repeated measurements. Observing the error variation curve generated via Xie's method, it can be seen that the error curve contains larger value fluctuations, indicating that Xie's method will contain errors in phase delay and modulation depth drift during the measurement process and is not corrected in time for them to be included in the measurement results. In comparing the experimental results in Figure 9, it can be known that the demodulation algorithm combined with Kalman filtering proposed in this paper is advantageous in suppressing parasitic interference. Xie's compensation method, although it can partially compensate for the effects of phase delay and modulation depth on the results, is unable to deal with the parasitic interference, as a result of which a slow amplitude drift and nonlinear error are introduced in the displacement measurement process. In contrast, the PGC phase demodulation algorithm based on Kalman filtering

significantly reduces the measurement error and can effectively suppress the effect of parasitic interference while ensuring the displacement measurement results. It is proved through experiments that the PGC phase demodulation algorithm exhibits higher stability and reliability during long-time measurements and can significantly improve the accuracy of displacement measurements. Compared with the four-sine and four-cosine carrier compensation methods, the PGC phase demodulation algorithm based on Kalman filtering is more suitable for combating interference in the environment. These results provide new ideas and methods for interference suppression in future optical measurement systems and provide strong support for improving measurement reliability and accuracy.

A comparison of the results of the error-corrected interferometer implemented in this paper with the results of other experiments can be seen in Table 2. The corrected error is reduced to 13 nm and on this basis, the measurement working range of the interferometer is greatly extended. However, the measurement accuracy of the interferometer has decreased, which is a disadvantage of the large working range.

Table 2. Performance of error-corrected interferometry results during dynamic measurements.

Error Correction Method	Working Distance/nm	Resolution/nm	Standard Deviation/nm
Four sine and four cosine carriers [16]	20	0.045	53.4
Kalman filter	200,000,000	40	13

To further elaborate on the experiment, it is essential to delve into the specific challenges posed by hysteresis and nonlinear effects in piezoelectric ceramic-based displacement stages. Hysteresis refers to the phenomenon where the output of the piezoelectric actuator depends not only on the current input signal but also on its history of excitation. This means that even if the input signal is the same, the output response may vary depending on previous states, leading to inaccuracies in positioning and control. Additionally, nonlinearities in the piezoelectric ceramic's behaviour can further complicate control efforts. These nonlinear effects can arise due to factors such as material properties, mechanical constraints, and electrical characteristics, making it difficult to establish a straightforward relationship between the input voltage and resulting displacement. By experimentally observing and quantifying these hysteresis and nonlinear effects, researchers can assess their impact on the performance of the displacement stage.

The analysis presented in Figure 10 highlights an important observation regarding the performance of the nano-displacement stage. While the ideal motion state of the stage is expected to exhibit uniform motion, the actual detected absolute displacement deviates from this ideal behaviour, displaying nonlinearity. This deviation provides evidence of the presence of the hysteresis phenomenon, indicating a nonlinear error in the movement of the displacement stage. By comparing the actual detected absolute displacement with the standard triangular wave curve, researchers are able to quantify the extent of the nonlinear error caused by the hysteresis phenomenon. The extreme value of this error is determined to be 0.4 μm , indicating the maximum deviation from the expected linear behaviour. This finding underscores the significance of addressing hysteresis effects in the design and control of nano-displacement stages. Strategies for mitigating hysteresis and minimising nonlinear errors are crucial for improving the accuracy and reliability of such stages in practical applications requiring precise motion control and positioning.

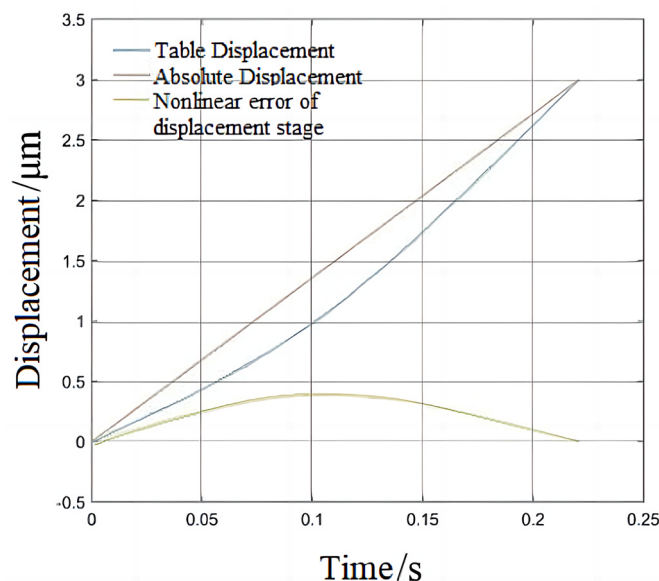


Figure 10. The actual absolute displacement of the nano-displacement stage during movement and the nonlinear error of the stage.

4. Conclusions

In this paper, an all-fibre low-finesse F–P interferometer with phase modulation based on Kalman filtering is proposed. For the parasitic interference problem faced in interferometer measurements, a Kalman filter is introduced to improve the demodulation algorithm and suppress the interference of parasitic interference. This paper analyses the interference and noise faced by signal demodulation in optical fibre interferometric systems and describes a Kalman filter-based PGC dephasing algorithm suitable for this interferometric system with respect to the characteristics of the interference. The algorithm adds the prediction process and update process of the characteristic parameters of the quadrature components of the Lissajous figure in the traditional PGC-Arctan process to avoid interference from entering into the arctangent operation.

The experimental results show that the interferometer, compared with previous interferometer devices, has a working distance in this paper increased to 200 mm and has better linearity. In the general environment, the resolution of the system reaches more than 10 nm, and the root mean square error is 0.0013 μm after the data are fitted to a straight line. Compared with other processing methods, the system in this paper can reduce the slow amplitude drift introduced by the parasitic interference in the displacement solution results and avoids the introduction of nonlinear errors in the displacement solution results. The realisation of the large working range of the interferometer makes it possible to measure the hysteresis phenomenon of the long-distance movement of the precision instrument and provides a basis for the compensation of the hysteresis error.

Author Contributions: Conceptualization, Y.W. and P.Y.; methodology, P.Y.; software, Y.W.; validation, P.Y. and Y.W.; formal analysis, P.Y.; investigation, Y.W.; resources, Y.W.; data curation, Y.W.; writing—original draft preparation, Y.W.; writing—review and editing, T.J.; visualization, T.J.; supervision, T.J.; project administration, T.J.; funding acquisition, T.J. All authors have read and agreed to the published version of the manuscript.

Funding: This research was funded by National Key R&D Program of China Grant No. [2023YFF1103405].

Data Availability Statement: The data presented in this study are available on request from the corresponding author due to the follow-up experiments in this laboratory will be updated and developed on this basis.

Conflicts of Interest: The authors declare no conflict of interest.

References

1. Tang, Y.; Li, L.; Wang, C.; Chen, M.; Feng, W.; Zou, X.; Huang, K. Real-Time Detection of Surface Deformation and Strain in Recycled Aggregate Concrete-Filled Steel Tubular Columns via Four-Ocular Vision. *Robot. Comput.-Integr. Manuf.* **2019**, *59*, 36–46. [CrossRef]
2. Peggs, G.N.; Yacoot, A. A Review of Recent Work in Sub-Nanometre Displacement Measurement Using Optical and X-Ray Interferometry. *Philos. Trans. R. Soc. Lond. Ser. A Math. Phys. Eng. Sci.* **2002**, *360*, 953–968. [CrossRef]
3. Calibration of a Scanning Probe Microscope by the Use of an Interference–Holographic Position Measurement System—IOPscience. Available online: <https://iopscience.iop.org/article/10.1088/0957-0233/14/7/318> (accessed on 25 March 2024).
4. Smith, D.T.; Pratt, J.R.; Howard, L.P. A Fiber-Optic Interferometer with Subpicometer Resolution for Dc and Low-Frequency Displacement Measurement. *Rev. Sci. Instrum.* **2009**, *80*, 035105. [CrossRef] [PubMed]
5. Yoshino, T.; Kurosawa, K.; Itoh, K.; Ose, T. Fiber-Optic Fabry-Perot Interferometer and Its Sensor Applications. *IEEE J. Quantum Electron.* **1982**, *18*, 1624–1633. [CrossRef]
6. Liu, M.; Yaraghi, N.; Xu, J.; Kisailus, D.; Mohideen, U. Compact Fiber Optical Interferometer Technique to Measure Picometer Displacements in Biological Piezoelectric Materials. *Meas. Sci. Technol.* **2020**, *31*, 025207. [CrossRef]
7. Liu, L.; Ren, Y.; Wang, M.; Zou, M. Optical Fiber Fabry-Perot Interferometer Sensor Fabricated by Femtosecond Laser-Induced Water Breakdown: Integrated Ferroelectrics. *Integr. Ferroelectr.* **2020**, *208*, 55–59. [CrossRef]
8. Islam, M.; Ali, M.; Lai, M.-H.; Lim, K.-S.; Ahmad, H. Chronology of Fabry-Perot Interferometer Fiber-Optic Sensors and Their Applications: A Review. *Sensors* **2014**, *14*, 7451–7488. [CrossRef] [PubMed]
9. Thurner, K.; Braun, P.-F.; Karrai, K. Fabry-Pérot Interferometry for Long Range Displacement Sensing. *Rev. Sci. Instrum.* **2013**, *84*, 095005. [CrossRef]
10. Meiners-Hagen, K.; Burgarth, V.; Abou-Zeid, A. Profilometry with a Multi-Wavelength Diode Laser Interferometer. *Meas. Sci. Technol.* **2004**, *15*, 741–746. [CrossRef]
11. Moro, E.A.; Todd, M.D.; Puckett, A.D. Performance Limitations of a White Light Extrinsic Fabry-Perot Interferometric Displacement Sensor. In *Fiber Optic Sensors and Applications IX*; SPIE: Baltimore, MD, USA, 2012; pp. 185–193.
12. Qi, B. Novel Data Processing Techniques for Dispersive White Light Interferometer. *Opt. Eng.* **2003**, *42*, 3165–3171. [CrossRef]
13. Jing, Z.; Yu, Q. Multiplexed Optical Fiber Extrinsic Fabry-Perot Interferometric Sensor System. *Proc. SPIE* **2006**, *6027*, 60274A. [CrossRef]
14. Nowakowski, B.K.; Smith, D.T.; Smith, S.T. Highly Compact Fiber Fabry-Perot Interferometer: A New Instrument Design. *Rev. Sci. Instrum.* **2016**, *87*, 115102. [CrossRef]
15. Sharma, S.; Eiswirth, P.; Petter, J. Electro Optic Sensor for High Precision Absolute Distance Measurement Using Multiwavelength Interferometry. *Opt. Express* **2018**, *26*, 3443–3451. [CrossRef]
16. Jin, T.; Wang, W.; Daul, L.; Koenders, L.; Hou, W. A Low-Finesse All-Fiber Sinusoidal Phase Modulation Interferometer for Displacement Measurement. *Opt. Commun.* **2021**, *493*, 126997. [CrossRef]
17. Zhang, Y.; Tian, X.; Liang, R. Random Two-Step Phase Shifting Interferometry Based on Lissajous Ellipse Fitting and Least Squares Technologies. *Opt. Express* **2018**, *26*, 15059–15071. [CrossRef] [PubMed]
18. Zhang, Y.; Tian, X.; Liang, R. Two-step random phase retrieval approach based on Gram-Schmidt orthonormalization and Lissajous ellipse fitting method. *Opt. Express* **2019**, *27*, 2575–2588. [CrossRef] [PubMed]
19. Park, S.; Lee, J.; Kim, Y.; Lee, B.H. Nanometer-Scale Vibration Measurement Using an Optical Quadrature Interferometer Based on 3×3 Fiber-Optic Coupler. *Sensors* **2020**, *20*, 2665. [CrossRef] [PubMed]
20. Zhang, X.; Mu, R.; Chen, K.; Yang, Y.; Chen, Y. Intelligent Hough Transform With Jaya to Detect the Diameter of Red-Hot Circular Workpiece. *IEEE Sens. J.* **2021**, *21*, 560–567. [CrossRef]
21. Liang, J.; Zhang, M.; Liu, D.; Zeng, X.; Ojowu, O.; Zhao, K.; Li, Z.; Liu, H. Robust Ellipse Fitting Based on Sparse Combination of Data Points. *IEEE Trans. Image Process.* **2013**, *22*, 2207–2218. [CrossRef] [PubMed]
22. Munir, M.; Siddiqui, S.A.; Dengel, A.; Ahmed, S. DeepAnT: A Deep Learning Approach for Unsupervised Anomaly Detection in Time Series. *IEEE Access* **2019**, *7*, 1991–2005. [CrossRef]
23. Wang, J.; Du, P.; Hao, Y.; Ma, X.; Niu, T.; Yang, W. An Innovative Hybrid Model Based on Outlier Detection and Correction Algorithm and Heuristic Intelligent Optimization Algorithm for Daily Air Quality Index Forecasting. *J. Environ. Manag.* **2020**, *255*, 109855. [CrossRef] [PubMed]
24. Zhang, D.; Peng, X.; Pan, K.; Liu, Y. A Novel Wind Speed Forecasting Based on Hybrid Decomposition and Online Sequential Outlier Robust Extreme Learning Machine. *Energy Convers. Manag.* **2019**, *180*, 338–357. [CrossRef]
25. Dong, Y.; Hu, P.; Ran, M.; Fu, H.; Yang, H.; Yang, R. Correction of Nonlinear Errors from PGC Carrier Phase Delay and AOIM in Fiber-Optic Interferometers for Nanoscale Displacement Measurement. *Opt. Express* **2020**, *28*, 2611. [CrossRef] [PubMed]
26. Xie, J.; Yan, L.; Chen, B.; Lou, Y. Extraction of Carrier Phase Delay for Nonlinear Errors Compensation of PGC Demodulation in an SPM Interferometer. *J. Light. Technol.* **2019**, *37*, 3422–3430. [CrossRef]
27. Guo, J.; Liu, X.; Hu, M.; Zhou, G. Elimination of Parasitic Interference Effect in Fiber-Optic External Sinusoidal Phase-Modulating Interferometer Based on Kalman Filter. *Measurement* **2022**, *187*, 110334. [CrossRef]
28. Cai, L.; Wang, J.; Pan, J.; Liu, Q.; Chen, Y. A Tunable Fiber-Optic Fabry-Perot Cavity Formed between a Silica Microsphere and a Target. *Opt. Commun.* **2020**, *459*, 124996. [CrossRef]

29. Yan, L.; Zhou, C.; Xie, J.; Chen, B.; Lou, Y.; Yang, T. Nonlinear Error Compensation Method for PGC Demodulation Based on Kalman Filtering. *Chin. J. Lasers* **2020**, *47*, 0904002. [[CrossRef](#)]
30. Karthick, R.; Senthilselvi, A.; Meenalochini, P.; Senthil Pandi, S. Design and Analysis of Linear Phase Finite Impulse Response Filter Using Water Strider Optimization Algorithm in FPGA. *Circuits Syst. Signal Process* **2022**, *41*, 5254–5282. [[CrossRef](#)]

Disclaimer/Publisher’s Note: The statements, opinions and data contained in all publications are solely those of the individual author(s) and contributor(s) and not of MDPI and/or the editor(s). MDPI and/or the editor(s) disclaim responsibility for any injury to people or property resulting from any ideas, methods, instructions or products referred to in the content.